

The root to the Galápagos mantle plume on the core-mantle boundary - supplementary materials

Sanne Cottaar^{1*}, Carl Martin¹, Zhi Li¹, Rita Parai²

1. Department of Earth Sciences, University of Cambridge, Cambridge, UK
 2. Department of Earth and Planetary Sciences, Washington University in St Louis, St Louis, MO, USA
- * corresponding author: sc845@cam.ac.uk

This PDF file includes:

Additional text

Figs. S1 to S14

Table S1

Other Supplementary Materials for this manuscript include the following:

Movies S1 to S4 – available at <https://doi.org/10.5281/zenodo.7105990>

1. Sdiff postcursor data set

Several further examples of events with postcursors are presented here. Fig. S1 shows the waveforms for an earthquake along the Chilean subduction zone on 2020/11/03. The event geometry is comparable to events A and B, and like with these events, postcursors are present presenting a moveout in time towards larger azimuths. The data for this event are very noisy, and the event is therefore excluded from further modelling. Additionally, the 1D synthetics show that the waveforms predicted are not a great fit, and the earthquake depth or the relative amplitudes between the direct and depth phases would have to be adjusted.

Postcursors caused by the Galápagos ULVZ are also seen after ScS phases. Fig. S2 shows an example of S/ScS waveforms in the 85-95° distance range from an earthquake at Easter Island recorded at stations in the United States and Canada. Postcursors in this distance range require further exploration and modelling beyond the scope of this study.

In Figs. S3 and S4, the geometry and waveforms are shown for three events in Alaska recorded across southern South America, which is a geometry largely opposite to events A and B. Waveform quality is generally poor and station coverage is sparser than in the opposite direction. Synthetic waveforms for the preferred ULVZ model are shown to suggest where postcursors might be present, and hints of these can be observed. Particularly the data for event T suggests a postcursor that appears further delayed in time than is observed in the

synthetic data. This could be evidence that the ULVZ needs to be more asymmetric than the simplified cylindrical model presented here.

2. Trade-offs in forward modelling

In the main paper we present our preferred cylindrical ULVZ model. Here we illustrate the sensitivity of the data to location, size, velocity reduction, and height of the model. Unlike several studies using diffracted data (Yuan and Romanowicz, 2017; Li, Sun and Bower, 2022), we have not been able to devise a quantitative measure to compare different models for several reasons. For event A, this is likely due to the overall poor waveform fit between the data and synthetic, which is controlled by the depth and source time function of the earthquake source and has not been optimized for this subset of data. For event B, the postcursor is weak and does not dominate any waveform misfit. For event C, we do not fit the amplitude of the postcursor well but fit the overall character. This could be due to our simplified model choices, or due to the assumed earthquake source. For event D, the data coverage is too poor to track and fit particular postcursors.

Forward modelling – location

The preferred cylindrical ULVZ model is centered at 105° W and 2° N, to the west of the Galápagos. Its location is constrained by having crossing ray paths from the different events. We illustrate this by presenting synthetics for shifted ULVZ models (Fig. S5) for event A (Fig. S6) and event C (Fig. S7). Event A samples the ULVZ from the southeast to the northwest, and synthetic models are presented shifted in these directions (labelled as SE and NW). In Fig. S6, we observe that the synthetic waveforms for these models remain comparable when shifted in these directions. Waveforms for synthetic models shifted in the orthogonal direction (labelled as SW and NE) show stronger variations in both postcursor moveout and amplitude.

For event C, the direction of propagation aligns the models SW and NW, and the models SE and NE. We observe little difference in the waveforms between SW and NW, or between SE and NE, but the move-out and amplitudes are very different between them. Postcursors for models to the west are offset towards smaller azimuth and for models to the east to larger azimuths than observed in the data. The combination of the two events thus constrains the best location within uncertainty of about 2°.

Forward modelling – size and velocity reduction

Size and velocity reduction are the least well constrained. Based purely on travel-times we expect strong trade-offs: a smaller and more reduced ULVZ predicts nearly the same postcursor travel time delays as a larger and less reduced ULVZ. When modelling we can observe more subtle waveform variations for differently sized ULVZs. Figs. S8 and S9 show

comparisons for different velocity reductions and ULVZ widths for events A and B. We compare modified models to the preferred model with a velocity reduction of 25% and a width of 600 km. In both cases, we observe that models with a weaker velocity reduction and a smaller width show a less strong move-out in the postcursors, while the move-out is too strong when the velocity reduction or width are increased. For event B, we also observe a strong variation in amplitude, with the postcursor almost disappearing for the weaker or smaller models.

More comparable waveforms can be obtained when both velocity reduction and width are varied inversely at the same time. Therefore, the uncertainties are the velocity reduction are at least 5% and the width is at least 100 km.

Forward modelling – height

To evaluate the height, we assess the data at longer periods between 30 to 50, as the synthetics for models of different heights show more variations in postcursor amplitudes at longer periods. At these periods, the amplitudes and travel-time delays of the observed postcursors are reduced. Event A (Fig. S10) still shows significant postcursors, but postcursors are barely visible for Events B and C (Figs. S11 and S12). This comparison is reproduced by synthetics with a ULVZ height of 20 km. For larger ULVZs, postcursor amplitudes increase significantly. There will be some trade-off with the overall size and velocity reduction of the ULVZ, and we expect equally fitting models can be found with 15 or 25 km thick ULVZs.

3. Beamforming results

For event A, we found 15 high quality stack windows for which the results are shown in Fig. 6, where they are compared to the results from the same stacking procedure on the synthetic data for our preferred ULVZ model. An example of a high-quality stack for event A is shown in Fig. S13. Event C has 13 high quality stacks for which 6 have a postcursor. Results for event C are shown in Fig. S14, comparing the results of observed stacks to those for the synthetic data of the preferred ULVZ model. In both cases, a bimodal distribution of peaks with time and backazimuth is observed. The synthetics for our preferred model slightly overpredict the difference in backazimuth between the main phases and the postcursors.

Event B has very little significant energy in the postcursor, as is also clear from the waveforms, and is therefore not further considered. Event D does not have sufficient coverage for stations with potential postcursors to consider stacking.

References

- Dziewonski, A. M. and Anderson, D. L. (1981) 'Preliminary reference Earth model', *Physics of the Earth and Planetary Interiors*, 25(4), pp. 297–356. doi: 10.1016/0031-9201(81)90046-7.
- Ekström, G., Nettles, M. and Dziewoński, A. M. (2012) 'The global CMT project 2004-2010: Centroid-moment tensors for 13,017 earthquakes', *Physics of the Earth and Planetary Interiors*, 200–201, pp. 1–9. doi: 10.1016/j.pepi.2012.04.002.
- French, S. W. and Romanowicz, B. A. (2014) 'Whole-mantle radially anisotropic shear velocity structure from spectral-element waveform tomography', *Geophysical Journal International*, 199(3), pp. 1303–1327. doi: 10.1093/gji/ggu334.
- Hauser, J., Sambridge, M. and Rawlinson, N. (2008) 'Multiarrival wavefront tracking and its applications', *Geochemistry, Geophysics, Geosystems*. John Wiley & Sons, Ltd, 9(11). doi: 10.1029/2008GC002069.
- Li, J., Sun, D. and Bower, D. J. (2022) 'Slab control on the mega-sized North Pacific ultra-low velocity zone', *Nature Communications*, 13(1), p. 1042. doi: 10.1038/s41467-022-28708-8.
- Yuan, K. and Romanowicz, B. (2017) 'Seismic evidence for partial melting at the root of major hot spot plumes.', *Science (New York, N.Y.)*. American Association for the Advancement of Science, 357(6349), pp. 393–397. doi: 10.1126/science.aan0760.

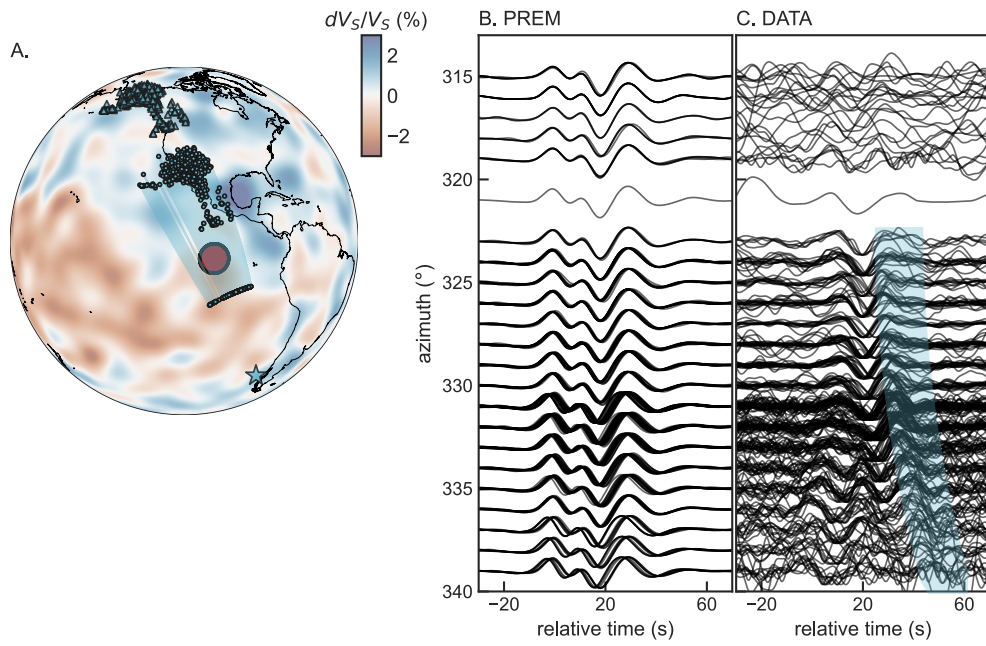


Fig. S1. Geometry and data for event on 2020/11/03.

(A) Map showing earthquake location (star), Sdiff paths in the lowermost mantle (shaded region) and stations (triangles). Preferred ULVZ shown in red. Background shows the shear wave velocity deviations at 2800 km depth from the tomographic SEMUCB-WM1 (French and Romanowicz, 2014). (B) Synthetic waveform predictions for PREM (Dziewonski and Anderson, 1981). (C) Observed waveforms. All waveforms are filtered between periods of 12.5 and 30 s. The geometry of this event is similar to event A and B in the main paper, but observations are noisier and the predicted waveforms are a poor fit.

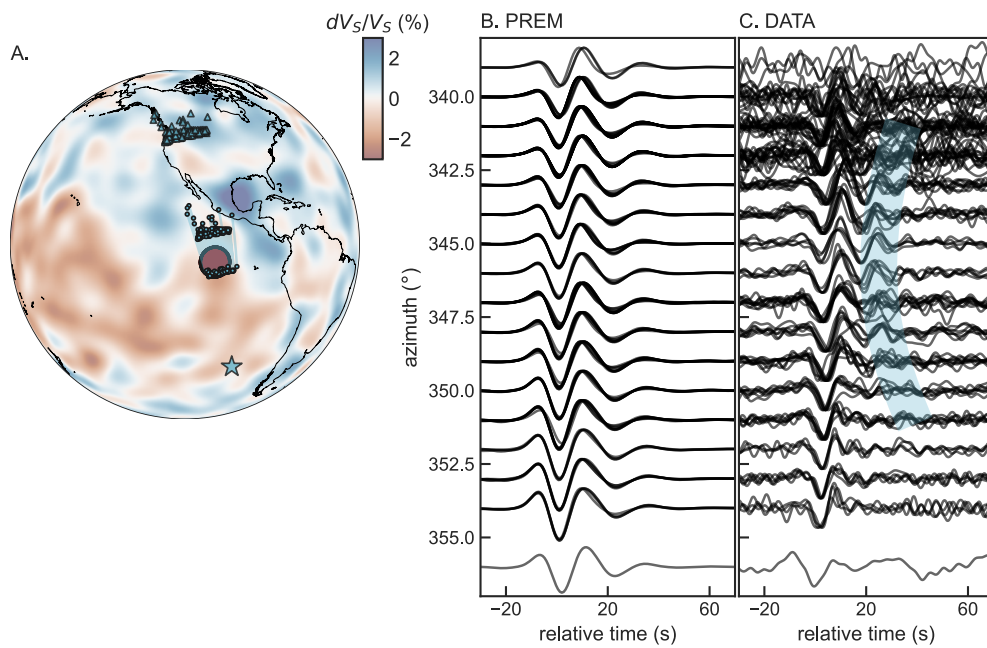


Fig. S2. Geometry and data for event on 2008/11/22.

(A) Map showing earthquake location (star), Sdiff paths in the lowermost mantle (shaded region) and stations (triangles). Preferred ULVZ shown in red. Background shows the shear wave velocity deviations at 2800 km depth from the tomographic SEMUCB-WM1 (French and Romanowicz, 2014). (B) Synthetic waveform predictions for PREM (Dziewonski and Anderson, 1981). (C) Observed waveforms. All data are filtered between 10 and 30s. Data for this event are in the 85-95° distance range and postcursors are present to the S/ScS phases. Presence of postcursors at these shorter distances requires further investigation.

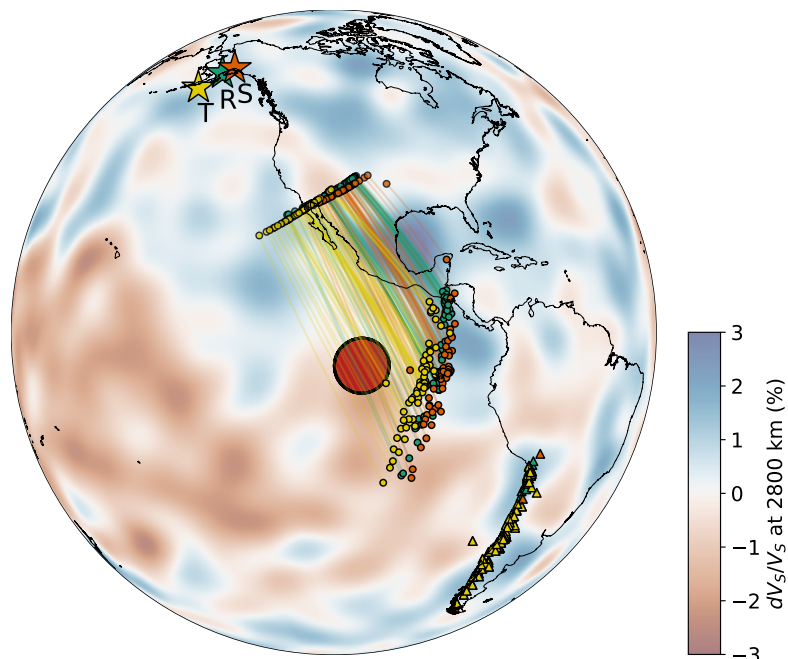


Fig. S3. Map of geometries for Alaska Events recorded in southern South America. Data geometries are shown by earthquake location (star), station locations (triangles), and ray path sensitivity to the core-mantle boundary (shaded regions between piercing points at 2800 km depth). Earthquake locations, ray paths and stations are coloured per event: R- cyan, S- orange, and T- yellow. The location of the Galápagos ULVZ, as constrained in this study, is shown as the red-filled circle. Background model shows the shear wave velocity deviations at 2800 km depth from the tomographic SEMUCB-WM1 (French and Romanowicz, 2014).

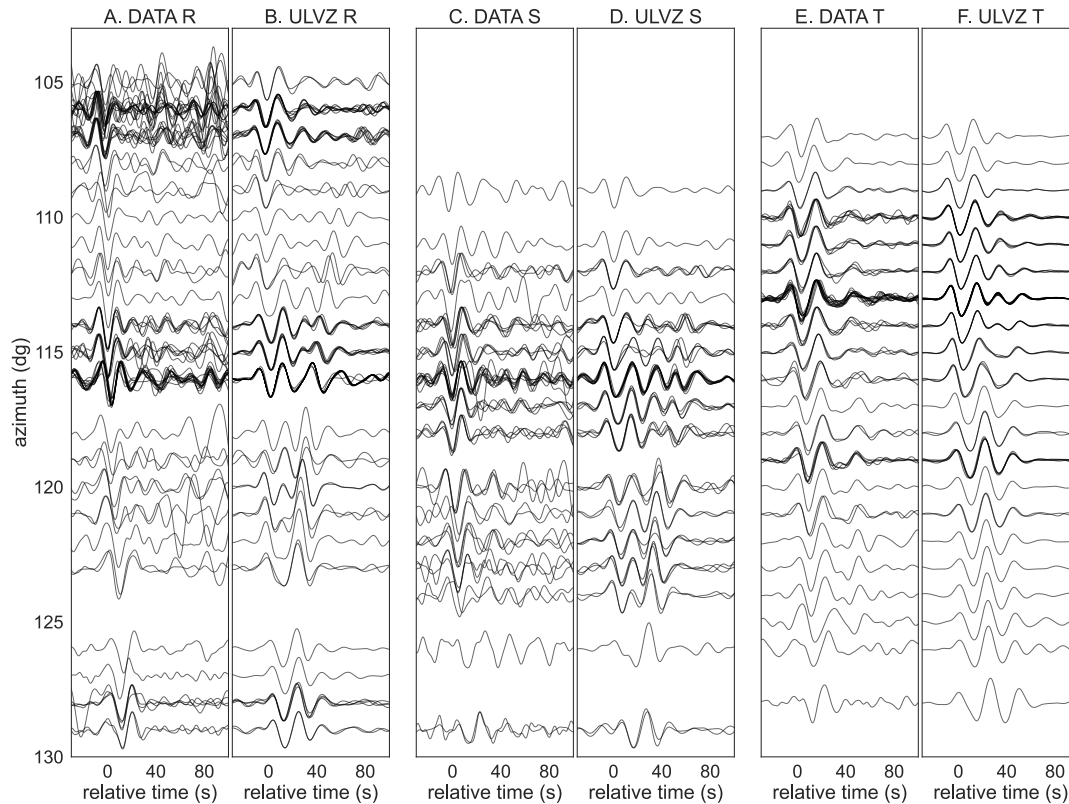


Fig. S4. Waveform data and synthetics for Alaska Events recorded in southern South America.

(A) Data for event R (2016/01/24) centered on the sSdiff phase, which is stronger than the main Sdiff phase for this event (B) corresponding synthetics for the preferred Galápagos ULVZ model. (C.) Data for event S (2018/11/30) centered on the sSdiff phase, which is stronger than the main Sdiff phase for this event (D) corresponding synthetics for the preferred ULVZ model. (E) Data for event R (2021/08/14) centered on the Sdiff phase, (F) corresponding synthetics for the preferred ULVZ model. All waveforms are filtered between 12.5 and 30 s. Data are relatively noisy, but hints of postcursors exist. Event T suggests the postcursor is further delayed than predicted by our preferred model.

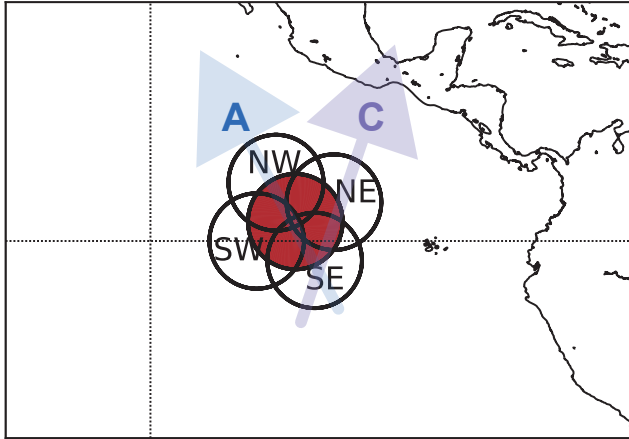


Fig. S5 Location shifts for the Galápagos ULVZ.

Reference preferred model is in red, centered at 105° W and 2° N. Shifted models are denoted as NW, NE, SE, and SW, indicating their shift directions. Arrows show the rough propagation direction for data for Event A (blue) and C (purple). ULVZ width of 600 km, height of 20 km, and shear wave velocity reduction of 25% are kept constant.

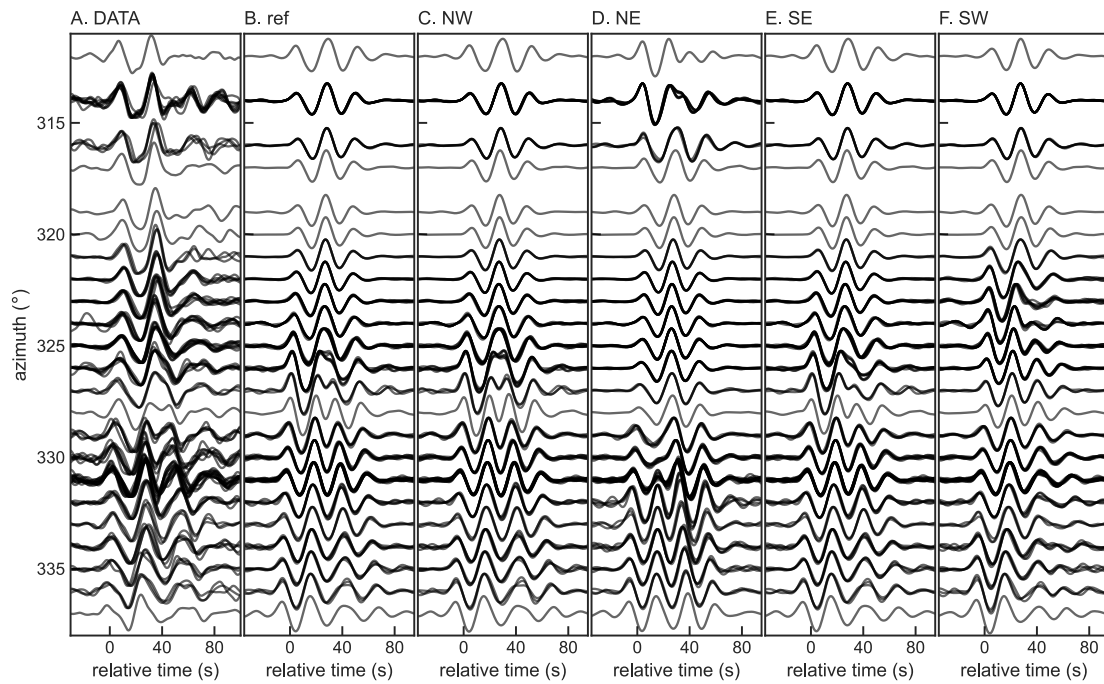


Fig. S6 Waveforms with location of the ULVZ for event A.

(A) Observed data for event A. (B) Synthetics for the preferred Galápagos ULVZ model. (C) Synthetics for preferred model shifted to the NW. (D) Synthetics for preferred model shifted to the NE. (E) Synthetics for preferred model shifted to the SE. (F) Synthetics for preferred model shifted to the SW. See locations in Figure S5. All waveforms are filtered between periods of 10 and 30 s.

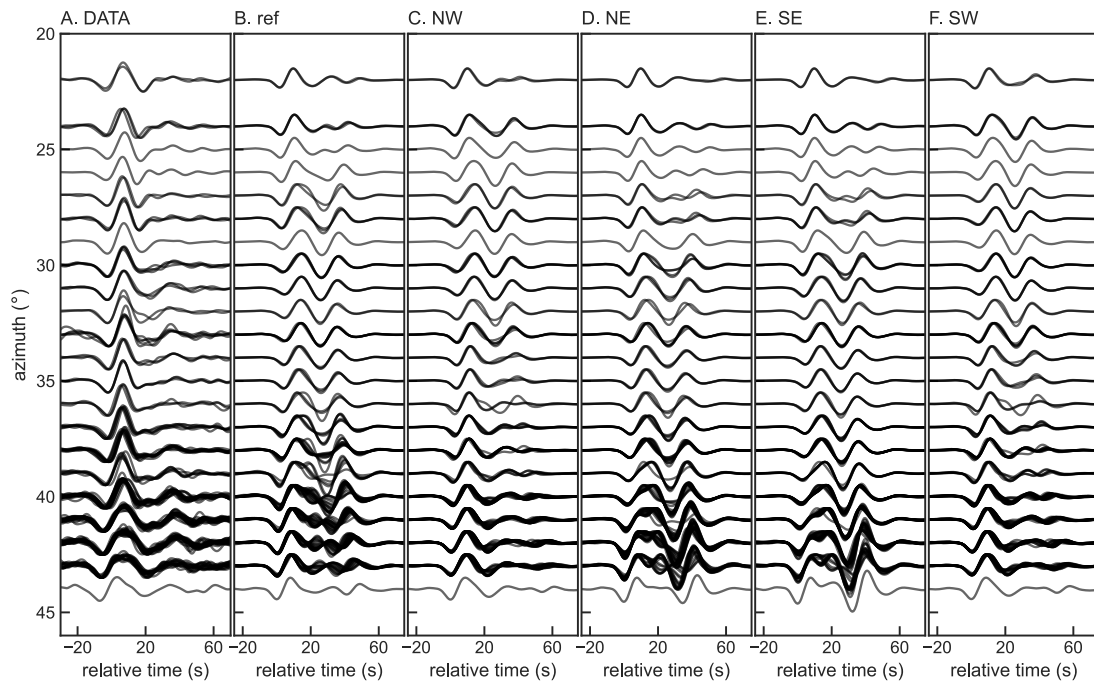


Fig. S7 Waveforms with location of the ULVZ for event C.

(A) Observed data for event C. (B) Synthetics for the preferred Galápagos ULVZ model. (C) Synthetics for preferred model shifted to the NW. (D) Synthetics for preferred model shifted to the NE. (E) Synthetics for preferred model shifted to the SE. (F) Synthetics for preferred model shifted to the SW. See locations in Figure S5. All waveforms are filtered between periods of 10 and 30 s.

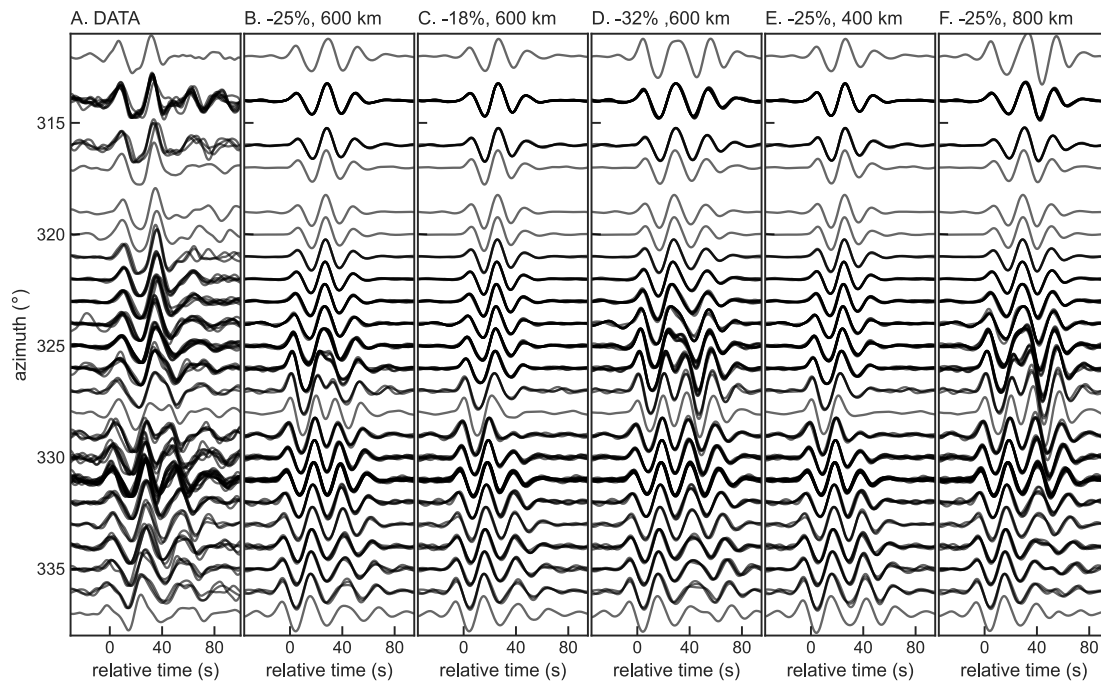


Fig. S8 Waveforms with varying velocity reduction and size of the ULVZ for event A. (A) Observed data for event A. (B) Synthetics for the preferred Galápagos ULVZ model with a shear velocity reduction of 25% and a width of 600 km. (C) Synthetics for model with a smaller velocity reduction of 18%. (D) Synthetics for model with a larger velocity reduction of 32%. (E) Synthetics for a model with a width of 400 km. (F) Synthetics for a model with a width of 800 km. All waveforms are filtered between periods of 10 and 30 s.

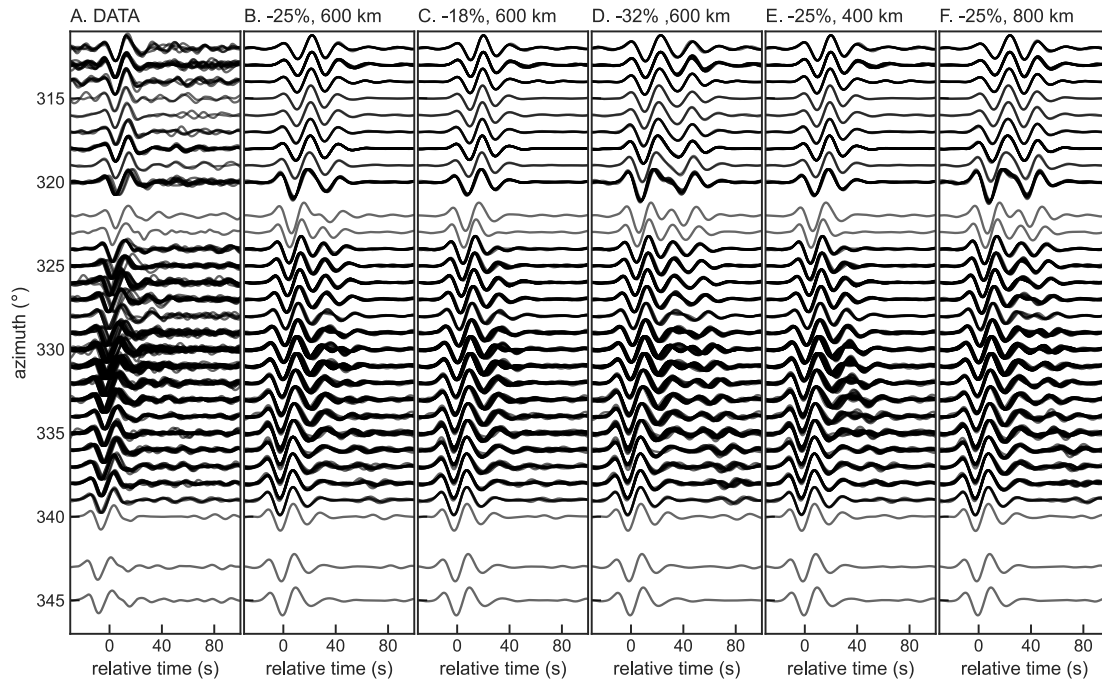


Fig. S9 Waveforms with varying velocity reduction and size of the ULVZ for event B. (A) Observed data for event B. (B) Synthetics for the preferred Galápagos ULVZ model with a shear velocity reduction of 25% and a width of 600 km. (C) Synthetics for model with a smaller velocity reduction of 18%. (D) Synthetics for model with a larger velocity reduction of 32%. (E) Synthetics for a model with a width of 400 km. (F) Synthetics for a model with a width of 800 km. All waveforms are filtered between periods of 10 and 30 s.

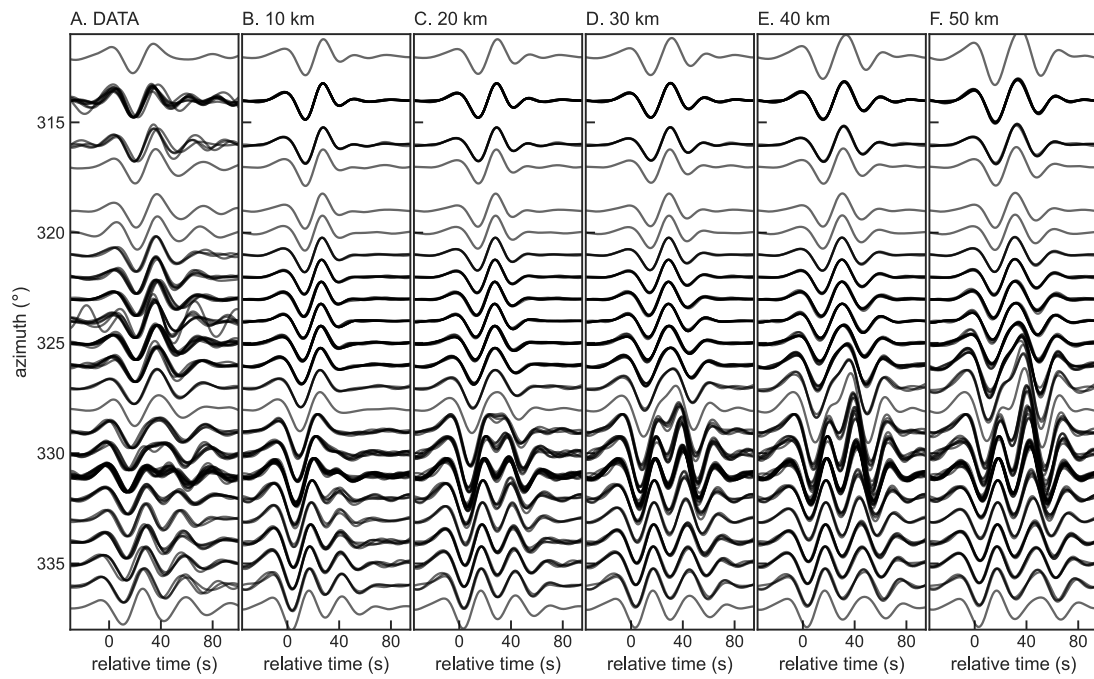


Fig. S10 Waveform predictions with height of the ULVZ for event A.

(A) Observed Sdiff waveforms. **(B-F)** Synthetic waveforms for ULVZs with a height of 10, 20, 30, 40, and 50 km. All waveforms filtered between periods of 30 and 50 s. The preferred model is 20 km in height.

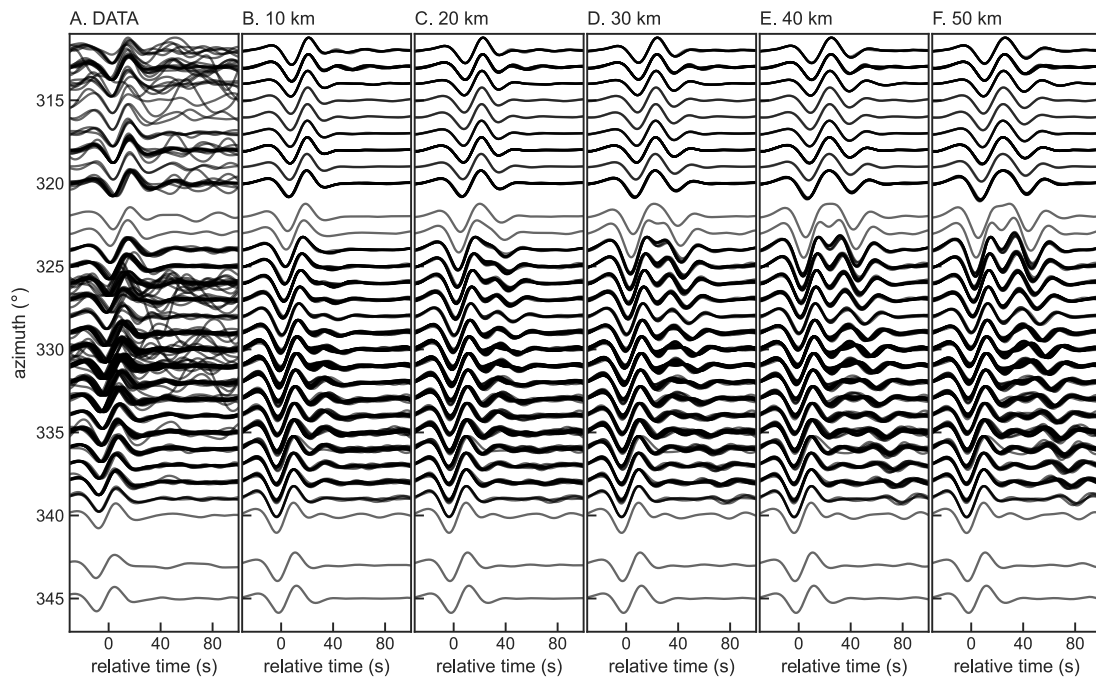


Fig. S11 Waveform predictions with height of the ULVZ for event B.

(A) Observed Sdiff waveforms for event B. **(B-F)** Synthetic waveforms for ULVZs with a height of 10, 20, 30, 40, and 50 km. All waveforms filtered between periods of 30 and 50 s. The preferred model is 20 km in height.

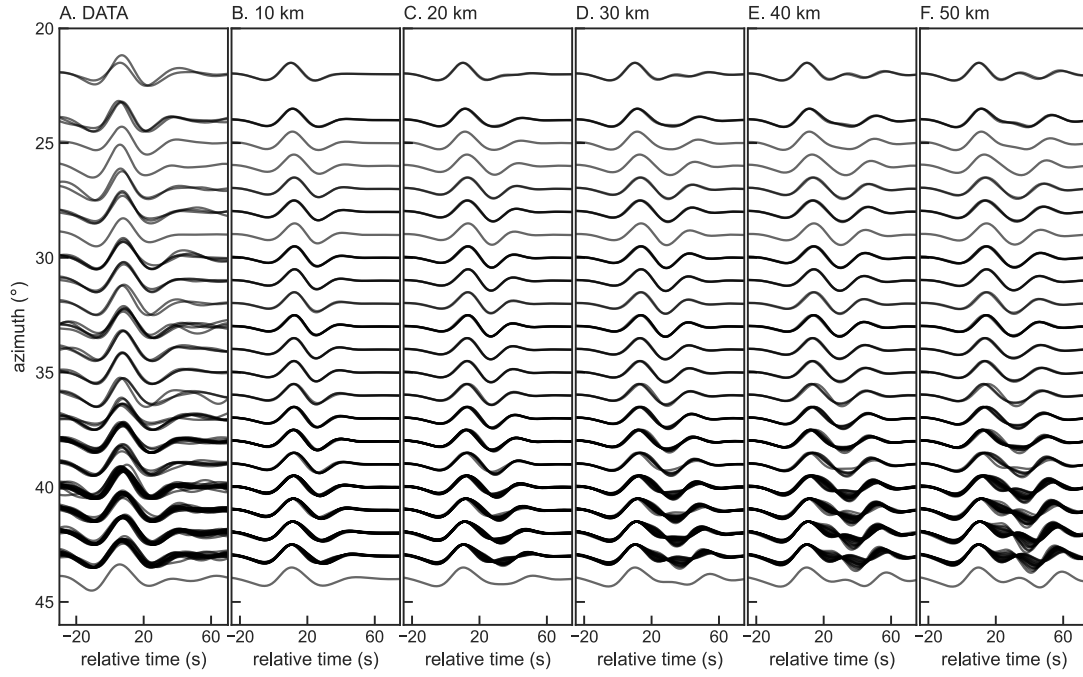


Fig. S12 Waveform predictions with height of the ULVZ for event C.

(A) Observed Sdiff waveforms for event C. **(B-F)** Synthetic waveforms for ULVZs with a height of 10, 20, 30, 40, and 50 km. All waveforms filtered between periods of 30 and 50 s. The preferred model is 20 km in height.

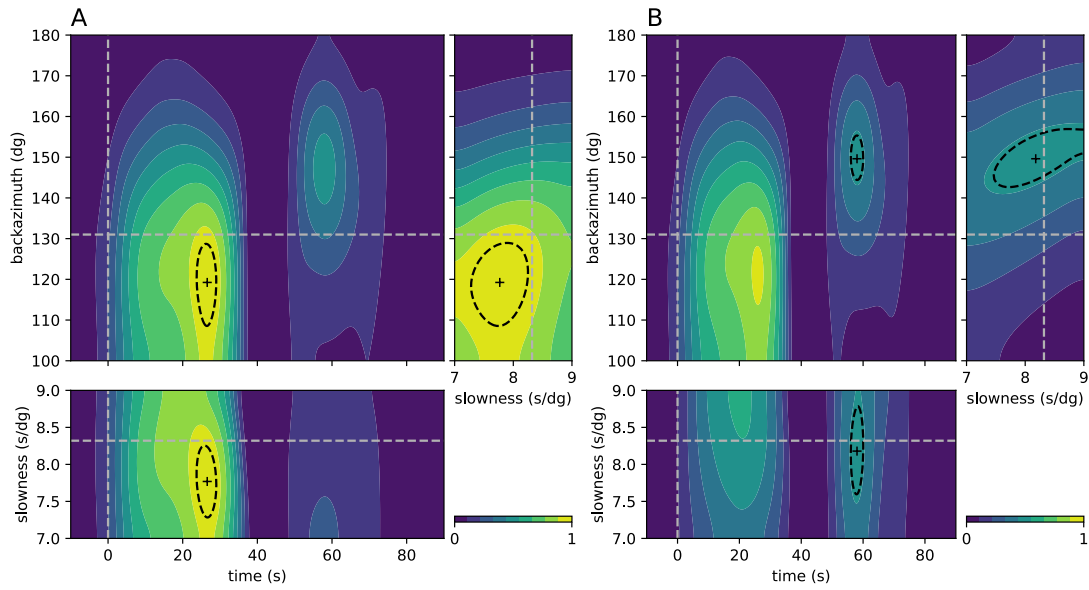


Fig. S13. Example of a normalized phase weighted envelope stack as a function of time, backazimuth, and slowness for a subset of 20 stations in Alaska for event A.

(A) Cross-sections are through the peak of the main Sdiff energy ($t = 27\text{s}$, $u_{hor} = 7.8\text{ S/o}$, $\theta = 119^\circ$). Black dashed lines show 95% contour around the peak used to pick the uncertainty. Grey dashed lines show reference time and slowness for an Sdiff wave in PREM (Dziewonski and Anderson, 1981), and the reference backazimuth from the center of the stack. **(B)** Same as (A), but for cross-section through the peak of the postcursor ($t = 58\text{ s}$, $u_{hor} = 8.2\text{ S/o}$, $\theta = 150^\circ$).

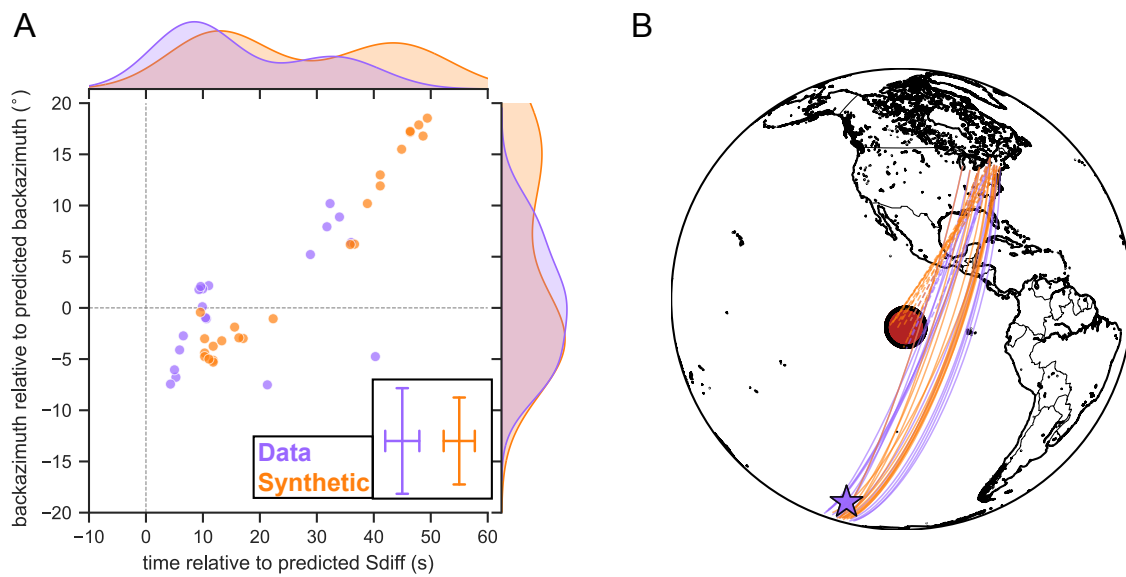


Fig. S14 Beamforming results for event C.

(A) Relative time vs. relative backazimuth for picked peaks in beamform stack for real data (purple) and synthetic data for the ULVZ model (orange). Error bars in lower right shows median uncertainty for the observations. **(B)** Back-projection of determined backazimuths for energy peaks. Solid lines represent the main Sdiff arrival (defined as arrivals before 25 s), while the dashed lines represent the Sdiff postcursors (arrivals after 25s).

Date	Dep [km]	Lat [°]	Lon [°]	Mw	Location
2021/08/14 - <i>T</i>	26	55.21	-157.42	7.0	ALASKA PENINSULA
2021/04/25	248	-21.70	-176.87	6.5	FIJI ISLANDS REGION
2021/04/24	315	-18.91	-176.13	6.6	FIJI ISLANDS REGION
2021/03/17	15	-41.40	-86.16	5.7	WEST CHILE RISE
2021/02/03	18	-36.38	-98.63	6.6	SOUTHEAST OF EASTER ISLAND
2020/11/03	18	-44.61	-79.46	6.0	OFF COAST OF SOUTHERN CHILE
2019/10/01	12	-56.13	-122.67	5.9	SOUTHERN EAST PACIFIC RISE
2019/09/29 - B	17	-35.56	-73.10	6.7	OFF COAST OF CENTRAL CHILE
2018/12/19	16	-36.17	-101.06	6.2	SOUTHEAST OF EASTER ISLAND
2018/11/30 - <i>S</i>	48	61.49	-150.02	7.0	SOUTHERN ALASKA
2017/07/04	12	-35.59	-73.56	5.9	OFF COAST OF CENTRAL CHILE
2017/02/24 - D	418	-23.44	-178.77	7.0	SOUTH OF FIJI ISLANDS
2016/12/25 - A	22	-43.41	-73.94	7.6	SOUTHERN CHILE
2016/08/18	13	-55.97	-123.63	6.0	SOUTHERN EAST PACIFIC RISE
2016/07/27	20	-44.62	-79.48	5.9	OFF COAST OF SOUTHERN CHILE
2016/01/24 - <i>R</i>	111	59.75	-153.27	7.1	SOUTHERN ALASKA
2015/06/20	12	-36.35	-74.10	6.4	OFF COAST OF CENTRAL CHILE
2015/05/19 - C	15	-54.53	-132.39	6.6	PACIFIC-ANTARCTIC RIDGE
2014/06/29	21	-55.34	-28.31	6.9	SOUTH SANDWICH ISLANDS REGION
2012/07/18	20	-55.36	-128.96	5.9	PACIFIC-ANTARCTIC RIDGE
2010/07/18	12	52.66	-169.64	6.7	FOX ISLANDS, ALEUTIAN ISLANDS
2010/05/20	12	-39.04	-92.33	5.9	SOUTHEAST OF EASTER ISLAND
2010/05/03	15	-38.31	-74.08	6.2	OFF COAST OF CENTRAL CHILE
2010/03/16	13	-36.49	-73.63	6.6	NEAR COAST OF CENTRAL CHILE
2010/03/05	15	-36.89	-73.75	6.6	NEAR COAST OF CENTRAL CHILE
2009/08/01	20	-55.70	-124.58	6.0	SOUTHERN EAST PACIFIC RISE
2008/11/22	12	-37.15	-95.29	5.7	SOUTHEAST OF EASTER ISLAND
2007/06/14	18	-36.22	-100.37	5.9	SOUTHEAST OF EASTER ISLAND
2007/05/07	20	-45.00	-81.21	6.0	OFF COAST OF SOUTHERN CHILE
2005/07/10	12	-36.38	-97.46	6.0	WEST CHILE RISE
2004/11/17	629	-19.87	-178.40	6.5	FIJI ISLANDS REGION
2004/07/15	577	-17.68	-178.52	7.0	FIJI ISLANDS REGION
2004/01/25	143	-16.75	-173.79	6.6	TONGA ISLANDS
2002/07/19	15	-57.07	-140.94	6.0	PACIFIC-ANTARCTIC RIDGE
1995/09/08	15	-56.15	-122.69	6.3	SOUTHERN EAST PACIFIC RISE

Table S1.

Earthquake event dates and parameters showing postcursor evidence in their ScS/Sdiff waves crossing the Galápagos ULVZ. Events in *bold+italic* are used in the main paper and A-D labels are included. Events in *italic* are shown in the supplements and R-T labels for events in Figures S3 and S4 are included. All earthquake parameters are for the Global Centroid-Moment Tensor project (www.globalcmt.org, (Ekström, Nettles and Dziewoński, 2012)) except for 2016/12/25-A, for which we use the W-phase solution published by the USGS National Earthquake Information Centre.

Movie S1.

Animation of interaction between the wavefront and the ultra-low velocity zone for Event A using a modified version of the wavefront tracker by (Hauser, Sambridge and Rawlinson, 2008). Only horizontal propagation is considered. Event location - blue star, seismometer locations – blue triangles. Velocities show the shear wave velocity deviations at 2800 km depth from the tomographic SEMUCB-WM1 (French and Romanowicz, 2014) and the ultra-low velocity zone.

Movie S2.

Animation of interaction between the wavefront and the ultra-low velocity zone for Event B using a modified version of the wavefront tracker by (Hauser, Sambridge and Rawlinson, 2008). Only horizontal propagation is considered. Event location - blue star, seismometer locations – blue triangles. Velocities show the shear wave velocity deviations at 2800 km depth from the tomographic SEMUCB-WM1 (French and Romanowicz, 2014) and the ultra-low velocity zone.

Movie S3.

Animation of interaction between the wavefront and the ultra-low velocity zone for Event C using a modified version of the wavefront tracker by (Hauser, Sambridge and Rawlinson, 2008). Only horizontal propagation is considered. Event location - blue star, seismometer locations – blue triangles. Velocities show the shear wave velocity deviations at 2800 km depth from the tomographic SEMUCB-WM1 (French and Romanowicz, 2014) and the ultra-low velocity zone.

Movie S4.

Animation of interaction between the wavefront and the ultra-low velocity zone for Event D using a modified version of the wavefront tracker by (Hauser, Sambridge and Rawlinson, 2008). Only horizontal propagation is considered. Event location - blue star, seismometer locations – blue triangles. Velocities show the shear wave velocity deviations at 2800 km depth from the tomographic SEMUCB-WM1 (French and Romanowicz, 2014) and the ultra-low velocity zone.